ISPRS Journal of Photogrammetry and Remote Sensing 159 (2020) 153–168

Contents lists available at ScienceDirect

ISPRS Journal of Photogrammetry and Remote Sensing

journal homepage: www.elsevier.com/locate/isprsjprs

An integrated photogrammetric and photoclinometric approach for illumination-invariant pixel-resolution 3D mapping of the lunar surface

Wai Chung Liu, Bo Wu*

Department of Land Surveying and Geo-Informatics, The Hong Kong Polytechnic University, Hung Hom, Kowloon, Hong Kong

ARTICLE INFO

Keywords:
Photogrammetry
Photoclinometry
Shape-from-shading
Image matching
Moon

ABSTRACT

High-resolution 3D information on lunar and planetary surfaces is crucial for planetary exploration missions and science. Photogrammetry is a state-of-the-art technology for generating 3D topographic models of surfaces such as digital elevation models (DEMs). The performance of the photogrammetry and the resulting DEMs is affected by image matching. However, most matching algorithms fail when the images have large differences in illumination and subtle textures. This problem can be addressed by integrating photoclinometry into the photogrammetric process. This paper presents an integrated photogrammetric and photoclinometric approach that is able to generate pixel-resolution DEMs of the lunar surface and is illumination invariant. The incorporation of photoclinometry into photogrammetry involves two main steps. First, a photoclinometry assisted image matching (PAM) approach is developed by integrating photometric stereo analysis in the image matching to create pixel-wise matches, even for images with large illumination differences. Second, the DEM derived from photogrammetry using the matching results is further refined to pixel-wise resolution using photoclinometry with a shadow constraint. The proposed approach has been used for high-resolution topographic mapping at the Chang'E-4 and Chang'E-5 landing sites using Lunar Reconnaissance Orbiter Camera (LROC) Narrow Angle Camera (NAC) images acquired under different illumination conditions. The results indicate that the proposed approach is robust to severe inconsistencies in illumination and subtle textures in cases where the conventional approaches fail. The approach is able to achieve geometric accuracies comparable to photogrammetry but more small-scale topographic details. The proposed approach can also be used for high-resolution topographic mapping of other planetary bodies such as Mercury or asteroids, and provides a useful reference for similar topographic mapping on Earth.

1. Introduction

Photogrammetry is a technology that allows 3D measurements of objects from photographs (Konecny, 1985; Heipke et al., 2007). Combining a variety of techniques, such as camera calibration, image matching, and bundle adjustment, photogrammetry is able to derive 3D information, e.g., point clouds and digital elevation models (DEMs), from a pair or set of overlapping images (Wu, 2017). In these techniques, image matching plays a vital role throughout the photogrammetric process. Dense and reliable image matching is a prerequisite for generating DEMs with favorable geometric accuracy and spatial resolution (Wu et al., 2011, 2012). However, this requires sufficient image texture and adequate similarities between the images. In the case of lunar and other planetary surfaces, images are often acquired under different illumination conditions. Significant differences in the illumination of remote sensing images can result in dissimilar image patterns of the same terrain surface, which in turn limits the use of these images and poses challenges to creating high-quality DEMs (Wu et al., 2012; Preusker et al., 2017).

Photoclinometry, or shape-from-shading (SfS), is another technology that reconstructs the 3D geometry (shape) based on the relationships between the image intensity (shading) and illumination and the viewing directions (Horn, 1977; Kirk, 1987). The intensity of each pixel contains information on the interactions between the incoming radiation (e.g., sunlight) and the surface. Photoclinometry then derives the surface gradients for each image pixel and estimates the underlying surface from its gradients. The technology can recover pixel-wise surface shapes from a single image (Grumpe et al., 2014; Wu et al., 2018a) or multiple images (Woodham, 1980; Liu et al., 2018), with the latter called photometric stereo.

However, although not favored in photogrammetry, varying illumination can provide the advantage of using photometric stereo for 3D

* Corresponding author.
E-mail address: bo.wu@polyu.edu.hk (B. Wu).

https://doi.org/10.1016/j.isprsjprs.2019.11.017
Received 16 August 2019; Received in revised form 11 November 2019; Accepted 19 November 2019
Available online 29 November 2019

surface reconstruction. Photometric stereo (Woodham, 1980) is an extension of photoclinometry in which images are simultaneously analyzed under different illumination conditions (e.g., images with sunlight coming from different directions) and the surface gradients are derived for each overlapping pixel. In contrast with the conventional image matching in photogrammetry, the overall reconstruction robustness of photometric stereo increases with the availability of inconsistent illuminations. Hence, this approach has the potential to be incorporated into image matching to handle severe differences in illumination and thus generate better matching results, which is impossible to achieve using the conventional image matching methods. In addition, photogrammetry can normally generate DEMs with resolutions only several times (e.g., 3–5 times, or greater) that of the original image resolution, depending on the textural condition of the image (Heipke et al., 2007; Wu et al., 2012). Photoclinometry can then be used to refine the photogrammetric DEMs such that they have resolutions comparable to the image resolution (Grumpe et al., 2014; Lohse and Heipke, 2004; Wu et al., 2018a).

This paper presents a novel approach to integrating photogrammetry and photoclinometry for the illumination-invariant 3D mapping of the lunar surface, which is able to generate pixel-wise resolution DEMs from images with large illumination differences. First, a photoclinometry assisted image matching (PAM) algorithm that is invariant to changes in illumination is presented. PAM is able to generate surface gradients from the candidate matching patches using photometric stereo reconstruction. Given that correct matches usually generate a reasonable surface while incorrect matches do not, PAM finds matches by evaluating the likelihood that they will generate a reasonable surface. The output of PAM is disparity maps that can be directly used to generate DEMs through photogrammetric intersection based on the image interior and exterior orientation parameters. Second, the photogrammetric DEM from the previous step is further refined by a photoclinometric technique (Wu et al., 2018a) such that a pixel-wise resolution of the DEM can be achieved. A new shadow constraint is also developed and incorporated into our existing photoclinometric framework (Wu et al., 2018a) for better performance.

The rest of the paper is organized as follows. Section 2 reviews the related literature. In Section 3, we provide detailed descriptions of the integrated photogrammetric and photoclinometric approach, PAM, and photoclinometric refinement. Section 4 presents experimental validations of the proposed approach using various Lunar Reconnaissance Orbiter Camera (LROC) Narrow Angle Camera (NAC) images covering the Chang'E-4 landing site and in the candidate Chang'E-5 landing region. Finally, concluding remarks are made in Section 5.

2. Related work

Image matching is a critical step in photogrammetry, and successful photogrammetric processing of remote sensing images requires accurate and sufficient matching points. The scale invariant feature transform (SIFT) algorithm (Lowe, 2004) is one of the most popular image matching methods used in the photogrammetry and computer vision communities. SIFT extracts the distinctive features of images and matches them according to descriptors constructed based on the intensities in the scale space. In images of the lunar and planetary surfaces, these descriptors usually correspond to topographic features such as boulders and crater rims. With SIFT and other feature-based algorithms, matching is only performed for the extracted feature points. For pixel-wise matching algorithms, semi-global matching (SGM) is a well-known method used for dense image matching (Hirschmüller, 2008). SGM requires images with epipolar geometry such that only the translational parameter (i.e., disparity) needs to be solved by matching. A number of matching cost functions are commonly used in SGM, such as the Birchfield and Tomasi measure (Hirschmüller, 2008; Wu et al., 2018b) and the rank transform and census transform order-based methods (Banz et al., 2012). However, most intensity-based matching methods fail when the images have obvious illumination differences (Grumpe et al., 2014), because the changes in illumination lead to complex changes in the intensities of the pixels and the subsequent image patterns (Wu et al., 2018b). To overcome this problem, several methods have been proposed for matching images with illumination differences. For example, the phase-correlation and phase-congruency methods were shown to be illumination invariant (Foroosh et al., 2002). Wu et al., 2018b presented an illumination-invariant SIFT by suppressing the descriptor based on the distribution of the dominant orientation of the feature points. However, this approach can only be used for feature matching. Other studies have addressed this problem by estimating the underlying surface gradients of each image using photoclinometry (Grumpe and Wöhler, 2011; Grumpe et al., 2014; Liu and Wu, 2018). As the surface gradients are supposed to be illumination-invariant representations of the image content, matching can be performed without encountering apparent difficulties related to the differences in illumination. The proposed PAM approach belongs to this group of methods, in that the matching is performed based on the surface gradients. However, whereas most other methods rely on the photoclinometric processing of individual monocular images, PAM jointly analyzes both images to directly create robust matches. As photoclinometry and photometric stereo reconstruction are able to perform pixel-wise estimation, PAM is able to perform pixel-wise matching and hence provides a good complement to the popular SGM framework, which is also a pixel-wise matching algorithm.

In regard to photoclinometry, Horn (1977, 1990) and Kirk (1987) proposed early algorithms for implementing photoclinometric surface reconstruction. Using a reflectance model, photoclinometry estimates the gradient of a surface by the ratio of the energy reflection embedded in the intensity value of each pixel. Reflectance models describe how a surface reflects energy from an illumination source to the observer. Popular reflectance models include the Lambert model, the Lunar-Lambert model (McEwen, 1991), the Hapke model (Hapke, 1981, 1986, 2002, 2012), and variants of the aforementioned models (Oren and Nayar, 1994; Labarre et al., 2017). Recent developments have also used low-order polynomial functions with in-situ data to simplify the complexity of the reflectance model (Wohlfarth et al., 2018). Photoclinometry produces DEMs and other types of 3D models with resolutions comparable to those of the input images, which are apparently higher than the models generated using methods such as photogrammetry and laser altimetry. The approach was further developed to be applied in planetary remote sensing (Kirk et al., 2003a; O'Hara and Barnes, 2012). For example, photoclinometrically derived products such as slope maps and DEMs were used for landing site assessment for Mars missions such as the Mars Exploration Rover missions (Beyer et al., 2003; Kirk et al., 2003b), Mars Science Laboratory mission (Beyer and Kirk, 2012), and the InSight mission (Beyer, 2017). Photoclinometry has also been used in lunar surface spectral analysis (Wöhler et al., 2014), lunar crater analysis (Salamunićcar et al., 2014), and mapping of geologic features (Wöhler et al., 2017). Although photoclinometry performs well on a local scale, it has poor accuracy on large scales. Hence, in recent years, methods have been developed to incorporate existing low-resolution 3D information (e.g., low-resolution DEMs from photogrammetry or laser altimetry) into photoclinometry (Grumpe et al., 2014; Wu et al., 2018a) and satisfactory results have been achieved. However, most of these approaches do not explicitly consider shadows. The shadows hide all of the intensity information needed for topographic reconstruction, thus leading to defective DEMs. This is particularly important for airless planetary bodies such as the Moon, because there is no atmosphere to scatter the light in other directions and illuminate the shadowed regions. Our proposed approach takes shadows into account in the photoclinometry to facilitate robust reconstruction around the shadows.

For photometric stereo, Woodham (1980) first proposed and demonstrated the use of multiple images, each under a different illumination condition, to estimate the surface gradients, which is referred to

as photometric stereo reconstruction. Multiple illuminations provide redundancy and hence allow more reliable determination of the surface. Photometric stereo reconstruction was applied to close-range and small-scale scene reconstruction (Ackermann et al., 2012; Jung et al., 2015). Heipke (1992) introduced the use of photometric stereo in topographic mapping, which is referred to as multiple-image shape-from-shading (MI-SfS) and applied the technique to earth observation images (Piechullek and Heipke, 1996; Piechullek et al., 1998). This approach was further developed and investigated for planetary mapping and surface reconstruction (Lohse and Heipke, 2004; Wöhler, 2004; Lohse et al., 2006; Liu and Wu, 2017; Liu et al., 2018). As photometric stereo requires corresponding pixels on all of the images, co-registration of the images is needed. As it is difficult to match and register images under different illumination conditions, image co-registration for photometric stereo usually requires different levels of manual work. In contrast, the proposed approach is able to automatically obtain pixel-synchronous images from the photogrammetric processing, which facilitates automatic photometric stereo reconstruction.

3. The integrated photogrammetric and photoclinometric approach

3.1. Overview of the approach

The workflow of the integrated photogrammetric and photoclinometric approach is illustrated in Fig. 1. The approach starts with a pair of lunar surface images with their corresponding exterior orientation (EO) parameters. The images may contain significant illumination differences. After epipolarly rectifying the images based on their EO parameters, the images are forwarded to the PAM algorithm to obtain the disparity maps. PAM is illumination-invariant and is able to match images with large illumination differences. A photogrammetric DEM is then generated using the disparity maps and the EO parameters of the images. Finally, the photogrammetric DEM is refined to pixel-resolution based on a photoclinometric method incorporating shadow constraint.

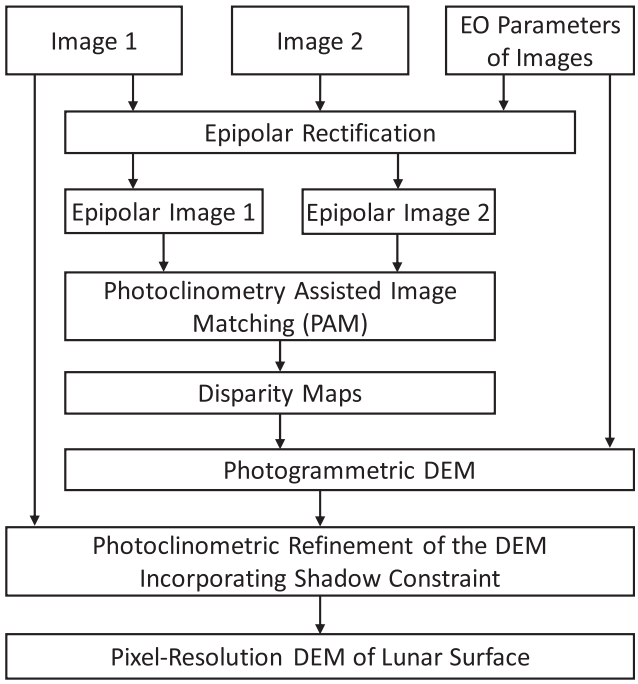

Fig. 1. Workflow of the integrated photogrammetric and photoclinometric approach.

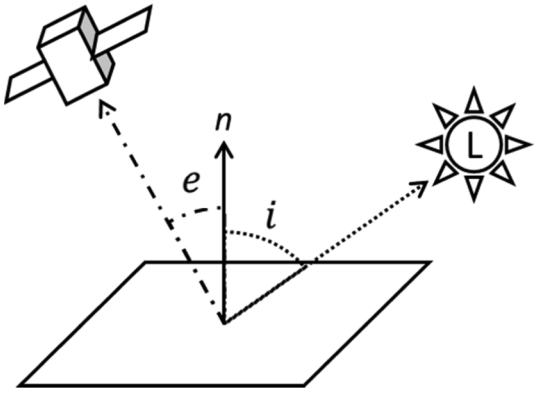

Fig. 2. Conceptual illustration of the relationships between the surface, the sun, and the observer (camera) for image acquisition.

3.2. Photoclinometry assisted image matching (PAM) invariant to illumination changes

3.2.1. Photometric stereo for image matching

Fig. 2 illustrates the photometric relationships for image acquisition on a surface. Assuming that a single light source from a certain direction illuminates the surface, the incidence angle (i) is formed between the vector pointing to the light source and the normal vector of the surface. The surface absorbs some of the light energy and reflects/scatters the remaining light in different directions. When an observer (e.g., a camera) is viewing from a certain direction, the emission angle (e) is formed between the vector pointing to the observer and the normal vector of the surface. Then, the amount of light received by the observer depends on (i) the incidence angle and the emission angle; and (ii) the surface reflecting properties (i.e., the intrinsic albedo).

Mathematically, the photometric relationships can be modeled as:

$$I = AG(p, q), \tag{1}$$

where the image intensity I is the product of the surface reflecting properties (i.e., albedo A) and the reflectance $G(p,q)$ generated from the surface $Z(x,y)$, and p and q denote the normal vector of the surface along the x-direction and y-direction, respectively. The normal vector of the surface is the negative of the surface gradients (i.e., $p = -\frac{\partial Z}{\partial x}$; $q = -\frac{\partial Z}{\partial y}$). The function $G(p,q)$ is also known as the reflectance model, which geometrically describes how a surface reflects incoming light from a source to an observer. In this paper, the Lunar-lambert model (McEwen, 1991) is used as follows:

$$G(p, q) = (1 - \lambda)\mu_0(p, q) + 2\lambda\frac{\mu_0(p, q)}{\mu_0(p, q) + \mu(p, q)}, \tag{2}$$

where μ_0 is the cosine of the incidence angle (i), μ is the cosine of the emission angle (e), and λ is the phase function which describes how the surface particles reflect light depending on the phase angle (i.e., the angle between the vector pointing to the light source and the vector pointing to the observer). Common models for the phase function in lunar and planetary photometry include the polynomial function (Lohse et al., 2006) and the exponential function (Gaskell, 2008).

If two images have been acquired of the same surface, they may or may not have consistent directions of illumination. It is quite common for images of lunar and planetary surfaces to have different illumination directions. Although matching images with different directions of illumination is difficult and not favored in photogrammetry, it can be achieved through photometric stereo as follows. Given the pixel intensity value of a point (x,y) on a base image ($I_B|_{xy}$) and the value of its corresponding pixel on the matching image (I_M), the ratio of the intensity values creates an albedo-free observation as follows:

$$\left.\frac{I_B}{I_M}\right|_{x,y} = \left.\frac{AG_B(p,q)}{AG_M(p,q)}\right|_{x,y} = \left.\frac{G_B(p,q)}{G_M(p,q)}\right|_{x,y}. \quad (3)$$

This is referred to as the quotient condition. Because the two pixels correspond to the same physical location, the intrinsic albedo $A_{x,y}$ of the pixels from the different images in this location should be the same. Hence, the differences are canceled out by division in Eq. (3). This method has been used for images with coplanar light sources (Wöhler, 2004) where the gradient along only one direction is estimated:

$$G(s) = G(sp_u, sq_u), \quad (4)$$

where s refers to the gradient along a predefined direction, and $\begin{bmatrix} p_u \\ q_u \end{bmatrix}$ is a unit vector denoting the predefined direction. Liu et al. (2018) used this approach to estimate the gradient along a predefined direction using the following quotient condition:

$$\left.\frac{G_B(s)}{G_M(s)}\right|_{x,y} = \left.\frac{I_B}{I_M}\right|_{x,y}, \quad (5)$$

where G_B and G_M are the reflectance functions (Eq. (4)) under the illumination and viewing conditions of the base image and matching image, respectively. The predefined direction is named the principal direction (Liu et al., 2018) and is determined according to Fig. 3. L1 and L2 are horizontal (azimuthal) vectors pointing toward each of the illumination sources, and v is a horizontal vector bisecting the angle L1-O-L2 such that $\angle a1 = \angle a2$. The principal direction u is determined by rotating vector v 90° clockwise. Our previous study (Liu et al., 2018) indicated that the ratio of reflectance (Eq. (5)) can be best represented along the principal direction because G_B and G_M behave in reverse manner as the gradient along this direction changes. Specifically, when the surface is inclined toward L1 (i.e., brighter G_B), its reflectance with respect to L2 will be lower (i.e., darker G_M), and vice versa, resulting in a wider spectrum of the ratio of reflectance as the gradient changes. However, for the gradient along the perpendicular of the principal direction (i.e., v), G_B and G_M change similarly as the gradient along v changes (i.e., both brighter or both darker). Thus, in this case, the ratio of reflectance will be close to constant as the gradient changes. As a result, the photoclinometric processing of both images along the principal direction will be more robust and less biased to any side, which will facilitate the subsequent photoclinometry assisted image matching.

A gradient map can be computed by solving for s in Eq. (5) at each pixel (x,y). Because the map presents the gradient along the principal direction (i.e., u in Fig. 3), it provides more topographic information along this direction and less information along its perpendicular (i.e., v in Fig. 3). Hence, the gradient changes more frequently along direction u and less frequently along direction v. This is similar to the situation in which an image shows more changes in intensity along the direction of illumination and less along its perpendicular.

Based on the aforementioned principles, we develop a PAM algorithm that is able to handle images with large differences in illumination. The concept of photometric stereo is used to calculate the matching score and evaluate the similarity of the candidate matches. In the process, the PAM algorithm finds matches by evaluating the underlying terrain instead of the direct image intensities. As a result, the differences in image intensity caused by the illumination differences do not significantly influence the matching.

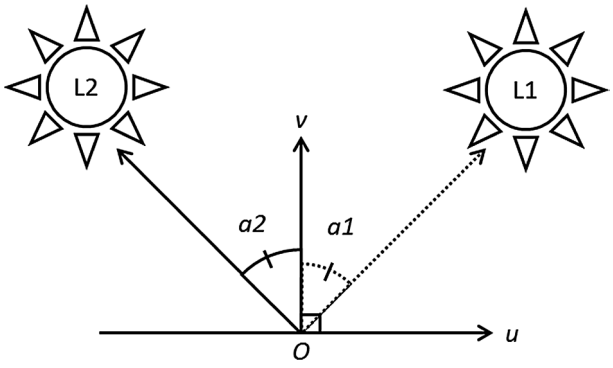

Fig. 3. Determination of the principal direction in photometric stereo. All vectors are on a 2D x-y plane.

The workflow of the PAM algorithm is illustrated in Fig. 4. Here, the design of PAM follows the general architecture of SGM (Hirschmüller, 2008), in which the base image (I_b) and matching image (I_m) are epipolarly rectified according to their EO parameters. The objective is to find the horizontal disparity dx and vertical disparity dy such that a pixel on the matching image $I_m(x + dx, y + dy)$ correctly corresponds to the pixel on the base image $I_b(x,y)$. Using disparities in two directions (x and y) ensures the matching is robust when the epipolar images are not perfectly aligned. For each pixel within a predefined disparity range (dx,dy), PAM extracts a local patch centered at $I_b(x,y)$ and $I_m(x + dx, y + dy)$. Using photometric stereo, PAM then analyzes the underlying terrain produced by the pair of image patches and generates a matching score representing the likelihood of the resulting terrain. The algorithm chooses the one with the highest matching score as the best match. PAM also considers the local smoothness and conducts multiple-scale evaluations when computing the matching score. Matches with significant changes in disparity are treated as mismatches and are filtered out, and the remaining matches are forwarded to the sub-pixel refinement. As the PAM algorithm incorporates the principle of photometric stereo, it requires the illumination directions with respect to the images to be known. This information can be obtained from the image metadata or derived by manual observation.

3.2.2. Computation of the matching score

For any local patch on the base image centered at pixel (x,y), a patch of the same dimension is extracted from the matching image with its center pixel translated by the disparities (dx,dy) under evaluation. A ratio of the two local patches is computed by dividing the patch on the base image by the one on the matching image. Using the ratio minimizes the effects of varying albedo in the photometric stereo analysis, as can be seen in Eq. (5). The photometric stereo technique is then used to determine the gradient map of the pair along the principal direction. The rationale behind PAM is that when the two image patches are matched correctly, they produce a highly reasonable gradient map due to the removal of the albedo variations by Eq. (5) and the accurate alignment of the corresponding pixels. However, when the two patches are matched incorrectly, they produce a biased gradient map due to misalignment. Biased gradient maps usually show similar roughness along multiple directions and have similar patterns of input images (influenced by the illumination), while reasonable gradient maps usually show high roughness only along the principal direction and low roughness along its perpendicular. Hence, the roughness of the gradient map can be evaluated along two orthogonal directions. The two directions are then combined using a mathematical function representing the matching score.

When a patch on the base image is matched with a candidate patch on the matching image, a gradient map can be generated using the aforementioned photometric stereo analysis. If the two patches are correctly matched, the gradient map is likely to have more frequent changes along the principal direction and less along its perpendicular. Otherwise, the map will have frequent changes along different directions due to “leakage” of the topographic and albedo information as a result of misalignment. PAM uses the gradient roughness to measure the changes. A reasonable gradient map is evaluated as having high gradient roughness along the principal direction and low gradient roughness orthogonal to the principal direction. The roughness of the gradient (s) map along direction t is evaluated using the following function:

$$S(s, t, \sigma)_{x,y,dx,dy} = g(s_{tt}^2, \sigma)_{x,y,dx,dy}, \quad (6)$$

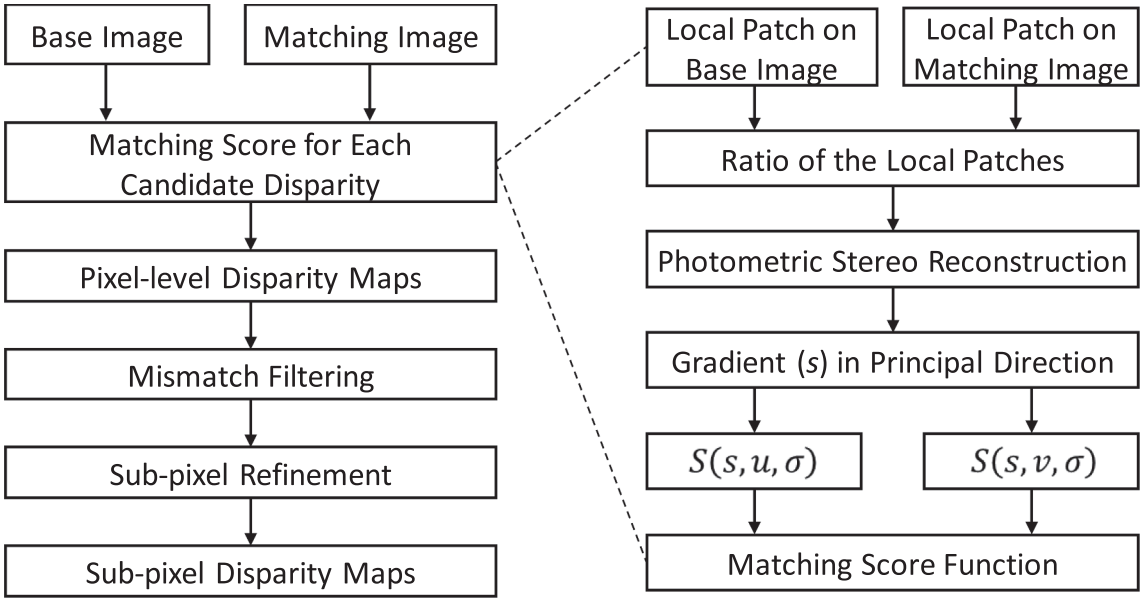

Fig. 4. The workflow of photoclinometry assisted image matching (PAM).

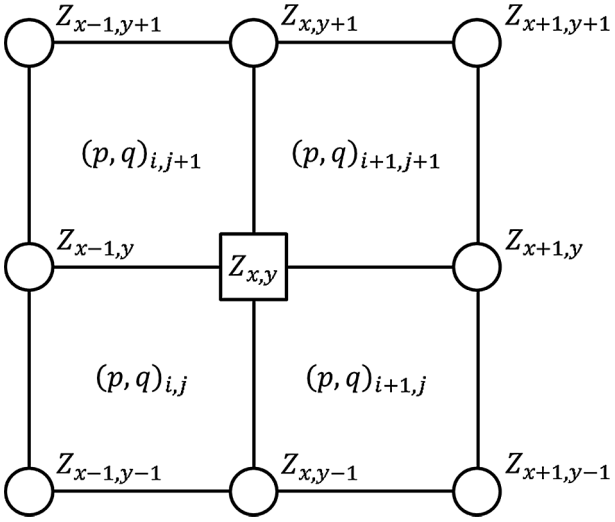

Fig. 5. The layout of a DEM node during height optimization. The center node is optimized according to the surrounding surface gradients.

where $S(s, t, \sigma)_{x,y,dx,dy}$ is the mean squared deviation of ${s_{tt}}^2$, the squared second derivative of s along the direction t, within a local region centered at pixel (x,y) with disparity (dx, dy). $g(*, \sigma)$ is a Gaussian function with the parameter σ controlling the size of the local region in the multiple-scale analysis and the relative contribution of each component within the region. ${s_{tt}}^2$ can be approximated by finite differences:

$${s_{tt}}^2 = (s_{t-1} - 2s_t - s_{t+1})^2. \tag{7}$$

A correct match is then defined as a high $S(s, u, \sigma)$ and a low (s, v, σ), of which u is the principal direction and v is its perpendicular. To achieve this, $S(s, u, \sigma)$ and $S(s, v, \sigma)$ are connected using a score function:

$$M(x, y, d_x, d_y, \sigma) = 1 - e^{-w_x S(s,u,\sigma)} + e^{-w_y S(s,v,\sigma)}|_{x,y,dx,dy}. \tag{8}$$

In the above function, the first component $1 - e^{-w_x S(s,u,\sigma)}$ increases when $S(s, u, \sigma)$ increases, while the second component$e^{-w_y S(s,v,\sigma)}$ penalizes a high$S(s, v, \sigma)$. w_x and w_y are weighting factors used to control the relative contribution of each component. A larger w_x and w_y mean the score is more easily affected by a small change in $S(s, u, \sigma)$ and $S(s, v, \sigma)$, respectively, and vice versa. M ranges from 0 to 2, with the best match approaching 2.

To ensure robustness of the matching score, PAM takes the multiple-scale evaluation into consideration by aggregating the matching scores computed from multiple image scales:

$$M_{final}(x, y, d_x, d_y) = \sum_{k \in K} M_k(x, y, d_x, d_y, \sigma_k), \tag{9}$$

where $M_k(x, y, d_x, d_y, \sigma_k)$ is the matching score at a scale denoted by σ_k within a predefined number K of scales. For computational consideration, this can be approximated by down-sampling the image by a factor (2 in this research) and computing the matching score for each down-sampled image. For each pixel (x,y), the disparities (dx,dy) with the highest matching score $M_{final}(x, y, d_x, d_y)$ are chosen as the best match.

3.2.3. Filtering of mismatches

Mismatches are unavoidable in most cases. In this paper, mismatches are defined as pixels with a disparity significantly different from their adjacent neighbors:

$$D_x(x, y) = |d_x(x, y) - d_x \in n| \geq \varepsilon$$

$$D_y(x, y) = |d_y(x, y) - d_y \in n| \geq \varepsilon, \tag{10}$$

where n is the vicinity of any pixel (x,y), and is defined as 1 pixel adjacent to the center pixel. ε is a predefined threshold default at 1. Eq. (10) is implemented by using morphological operators on the disparity maps:

$$D_x(x, y) = |morph_{dil}(d_x(x, y), n) - morph_{ero}(d_x(x, y), n)|$$

$$D_y(x, y) = |morph_{dil}(d_y(x, y), n) - morph_{ero}(d_y(x, y), n)|, \tag{11}$$

where $morph_{dil}(*, n)$ is a dilation operator whereby the value of a pixel is replaced by the highest value within a neighborhood defined by n, and $morph_{ero}(*, n)$is an erosion operator whereby the value of a pixel is replaced by the smallest value within the neighborhood. The neighborhood is defaulted as a 3x3 kernel, which means that only the disparities of the adjacent pixels are compared. A pixel is labelled as a mismatch when $D_x(x, y) \geq \varepsilon$ or $D_y(x, y) \geq \varepsilon$. Pixels enclosed by mismatches are also labelled as mismatches, which can be achieved by using an algorithm such as flood fill or watershed analysis. After filtering the mismatches, the sub-pixel values of the matches are estimated by fitting a quadratic curve over the matching score of the

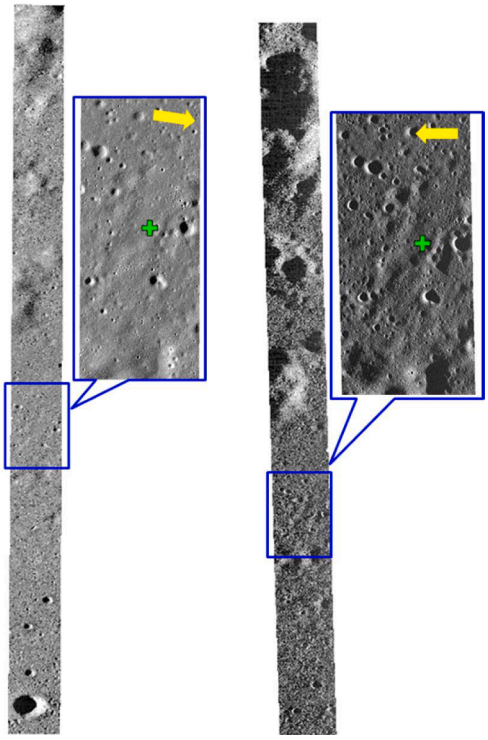

M134022629LC M178833263LC

Image ID	M134022629LE	M1145135367L
Slew angle (°)	0.0	-22.1
Illumination azimuth (°)	282.4	86.2
Incidence angle (°)	77.6	86.7
Emission angle (°)	1.7	23.0
Resolution (m/pixel)	1.3	1.4

Fig. 6. The LROC NAC image pair covering the Chang'E-4 landing site. Blue boxes show the enlarged views of the landing area, and green crosses indicate the landing site on each of the images. Yellow arrows indicate the illumination direction of each image. (For interpretation of the references to colour in this figure legend, the reader is referred to the web version of this article.)

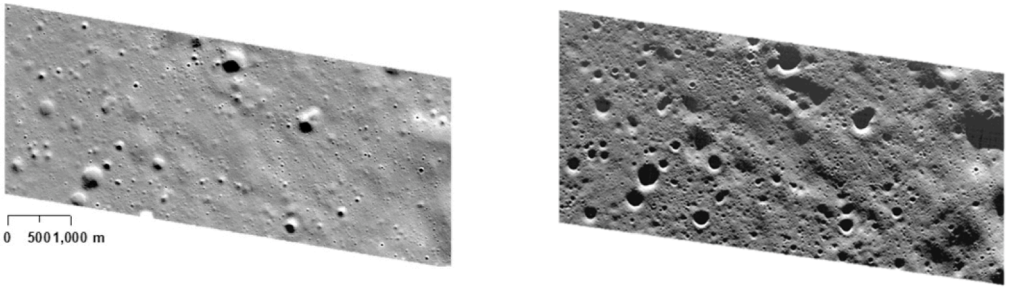

a) The base image (left) and the matching image (right)

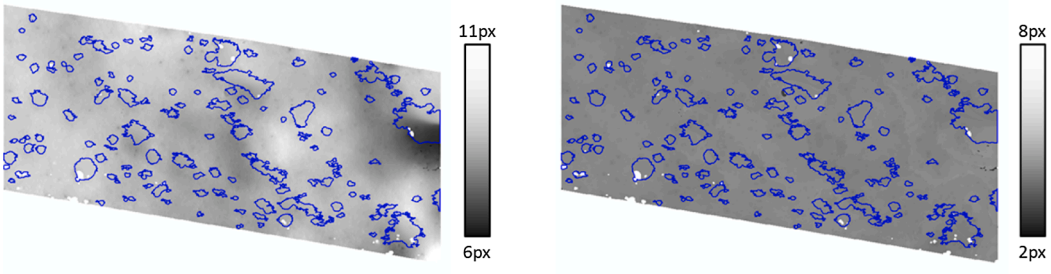

b) The x-disparity (left) and y-disparity (right) map.

Fig. 7. The epipolar images used for matching and the disparity maps generated by PAM for the Chang'E-4 landing site. Poor matches are outlined in blue. (For interpretation of the references to colour in this figure legend, the reader is referred to the web version of this article.)

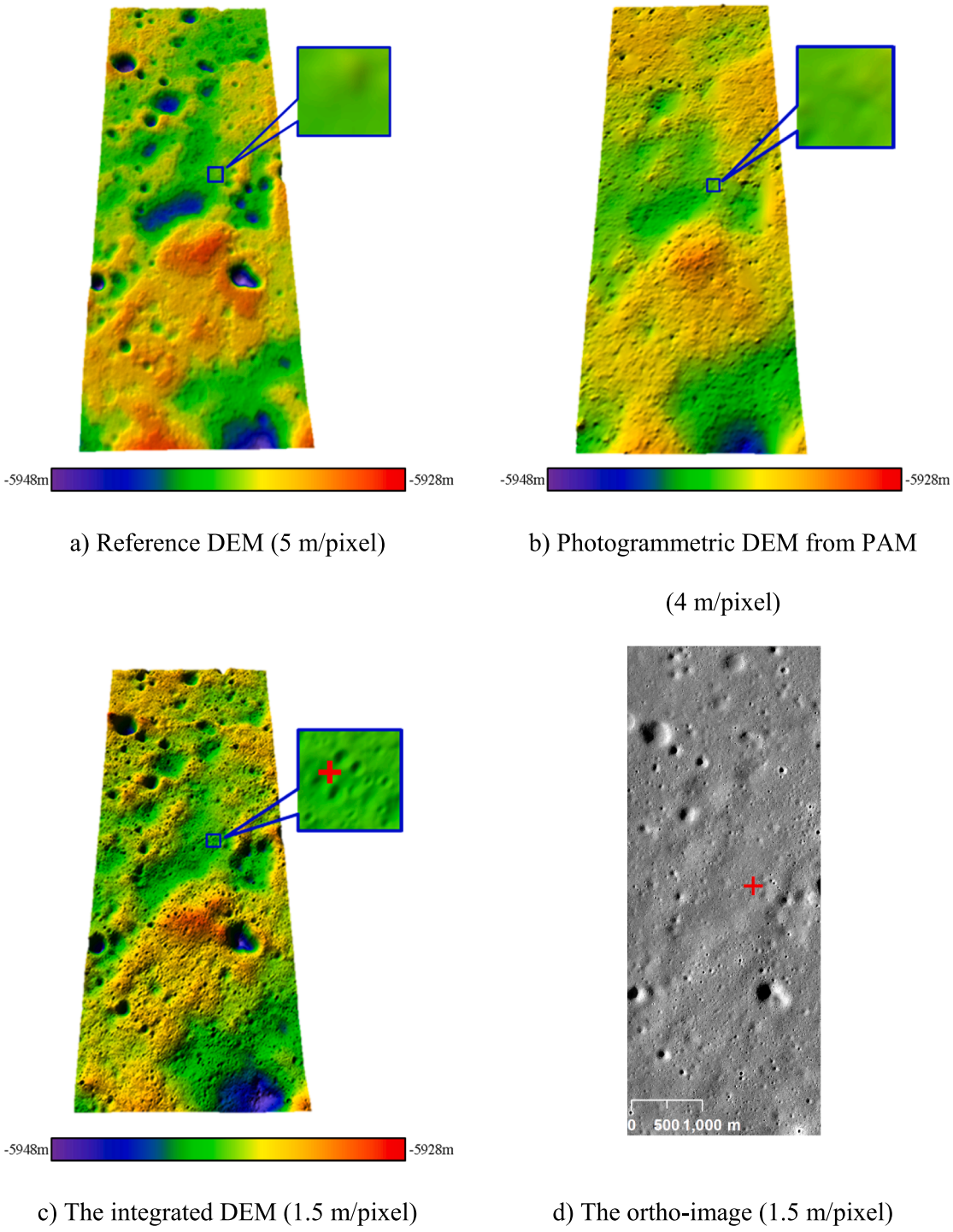

Fig. 8. 3D views of the DEMs and the corresponding ortho-image covering the Chang'E-4 landing site. The blue boxes show close up views of the landing site (the red cross). (For interpretation of the references to colour in this figure legend, the reader is referred to the web version of this article.)

neighboring disparities and finding the minima (Hirschmüller, 2008).

3.3. Photoclinometric refinement of photogrammetric DEM incorporating shadow constraint

3.3.1. Surface gradients from image intensities constrained by photogrammetric DEM

Using the above matching results from PAM, a photogrammetric DEM can be generated based on the EO parameters. Single-image SfS is then used to recover details that exist on the image but not in the photogrammetric DEM. Only one image of the stereo pair is needed for this process. Hence, the image with better illumination conditions, such as fewer shadows and adequate topographic shading, is chosen. Similar to Grumpe et al., 2014; Wu et al., 2018a, the SfS algorithm introduces a low-resolution DEM (i.e., the photogrammetric DEM) as a constraint and generates a high-resolution DEM with comparable resolution and details to the image. The image used in the SfS is co-registered to the photogrammetric DEM by ortho-rectification based on the image EO parameters. In Wu et al., 2018a, the reflectance of a pixel is estimated from its neighboring pixels by assuming locally constant albedo, yielding an albedo-free equation:

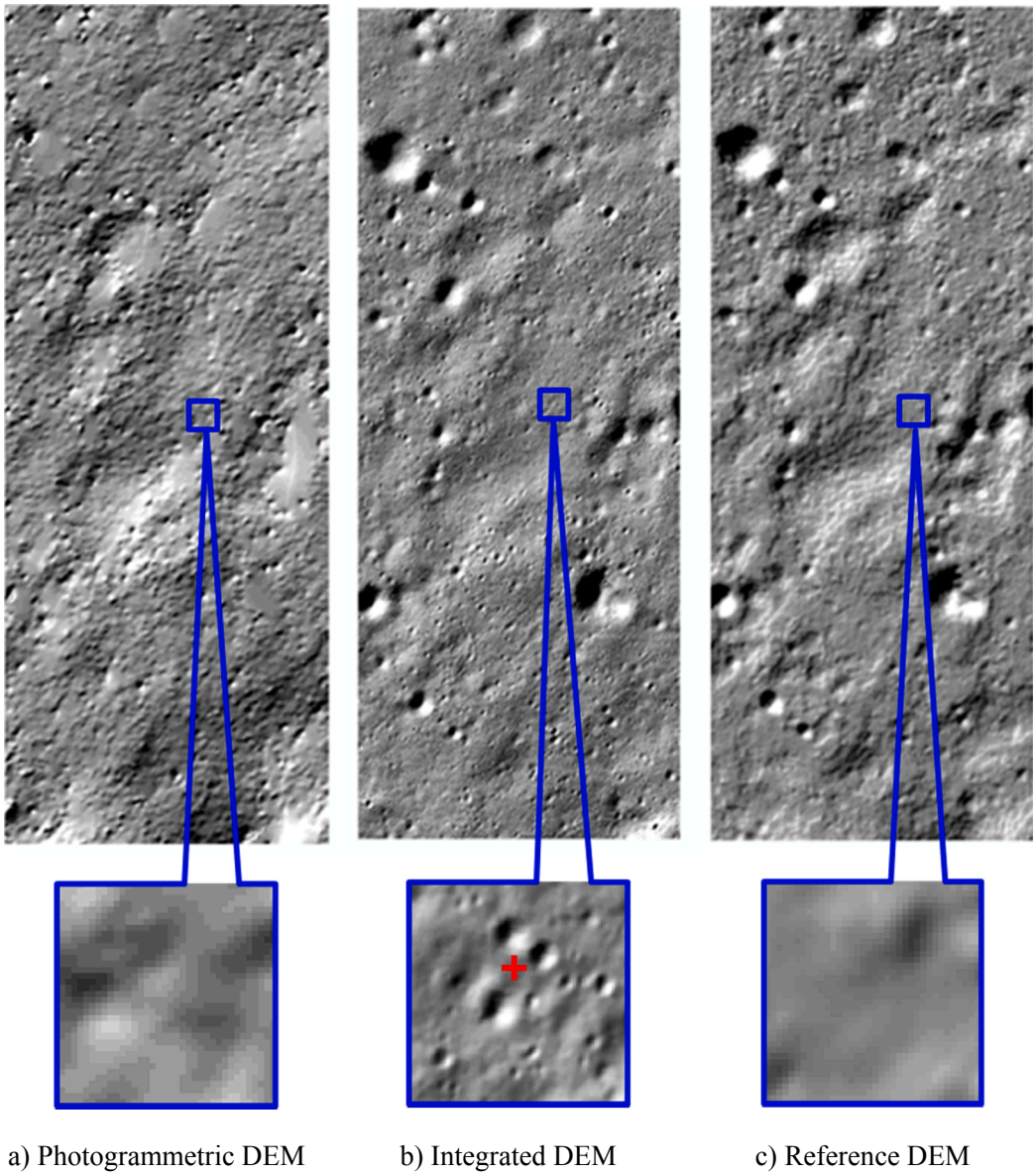

Fig. 9. The shaded relief of the DEMs covering the Chang'E-4 landing site. The blue boxes show close up views of the landing site (the red cross). (For interpretation of the references to colour in this figure legend, the reader is referred to the web version of this article.)

$$\left.\frac{A_{x,y}G_{x,y}}{A_jG_j} = \frac{I_{x,y}}{I_j}\right|_{j\in N}$$

$$G_{x,y} = \frac{I_{x,y}}{n}\sum_{j\in N_{x,y}}\frac{G_j}{I_j}, \tag{12}$$

where each I_j is an image pixel within a predefined local neighborhood $N_{x,y}$ of the center pixel $I_{x,y}$. It is assumed that the albedo at the center $A_{x,y}$ equals the A_j of its vicinity, and hence that the ratio of the reflectance value equals that of the image intensity. The estimated reflectance $G_{x,y}$ is then computed as the mean of all of the valid candidate reflectance values $\frac{I_{x,y}}{I_j}G_j$within $N_{x,y}$. The shadowed regions are not considered as valid pixels in this process. The reflectance value of each pixel is initialized from the initial DEM, with the values being derived from the photogrammetric DEM in this case. The normal vectors along the x-direction (p) and y-direction (q) are then obtained by minimizing:

$$E_{sfs} = G(p_0, q_0)|_{x,y} + \frac{\partial \mathrm{G}}{\partial \mathrm{p}}\Delta p + \frac{\partial G}{\partial q}\Delta q - G_{x,y}, \tag{13}$$

where p_o and q_o are the surface gradients of the DEM at the current iteration and Δp, Δq are the update values for the surface gradients. The photogrammetric DEM serves as the initial DEM for the initial conditions and constraints during the refinement. Wu et al., 2018a incorporate the initial DEM constraint by a cost function:

$$F(p, q) = (p - p_0)^2 + (q - q_0)^2 + w_{ini}[(g(p, \sigma) - p_{ini})^2 + (g(q, \sigma) - q_{ini})^2]. \tag{14}$$

The first two components, which are referred to as the integrability constraints (Horn, 1990), encourage the surface normal vectors to approach the closest integrable solutions p_o and q_o of the current iteration. The last two components, which are referred to as the initial DEM constraints, encourage the low-resolution versions of the normal vectors (i.e., $g(p, \sigma)$ and $g(q, \sigma)$) to approach those of the initial DEM (i.e., p_{ini} and q_{ini}). w_{ini} controls the contribution of the initial DEM constraint. The reflectance constraint E_{sfs} is treated as an absolute constraint, which separates the more important E_{sfs} from the other geometrical constraints $F(p,q)$ and ensures its effect. p and q are then updated using

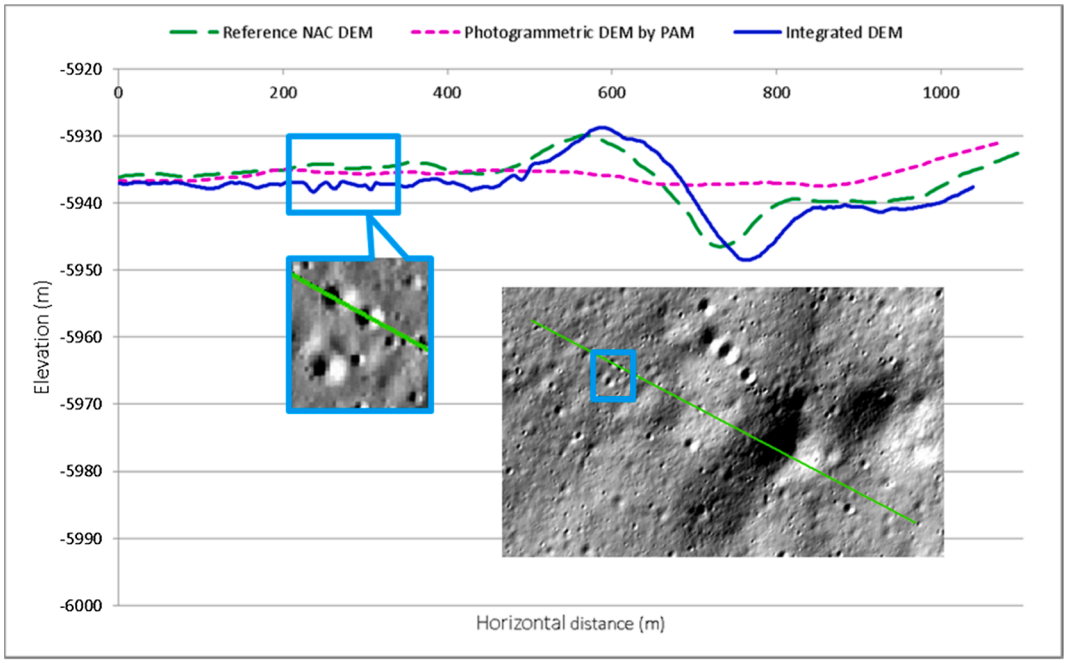

a) Profile 1

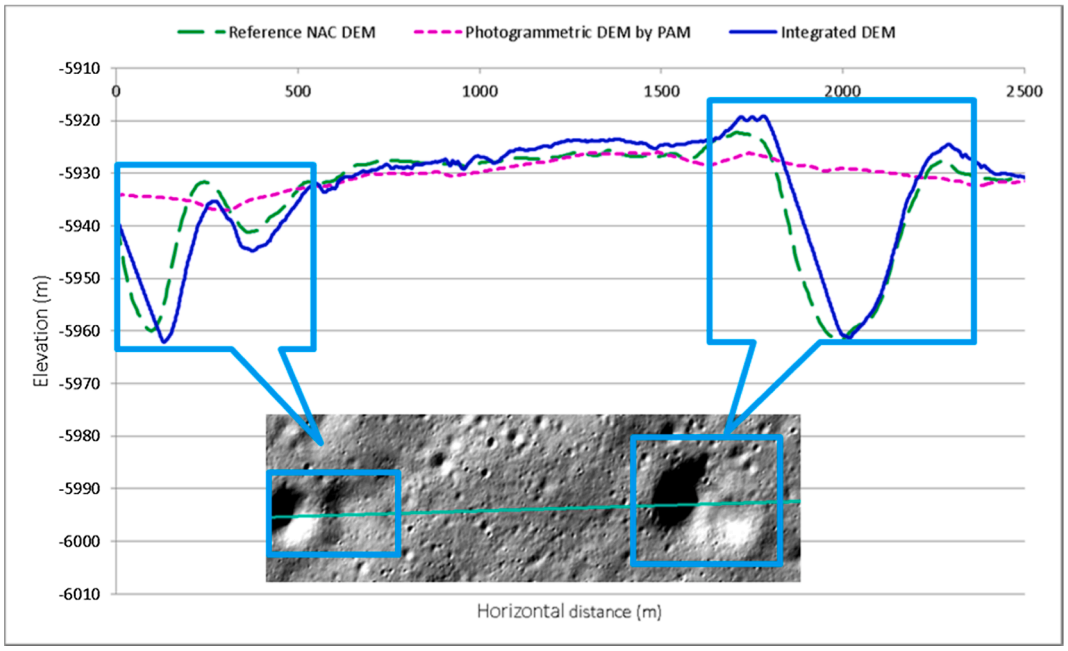

b) Profile 2

Fig. 10. Profile comparison of the DEMs of the Chang'E-4 landing site. The blue boxes indicate the topographic details revealed by the integrated DEM. (For interpretation of the references to colour in this figure legend, the reader is referred to the web version of this article.)

Table 1
Comparative statistics of the DEMs of the Chang'E-4 landing site.

	Photogrammetric DEM	Integrated DEM
RMSE (m)	4.32	3.47
Maximum absolute deviation (m)	38.49	19.84
Absolute deviation at 99.5 percentile (m)	21.66	11.17

the Lagrange multiplier (Wu et al., 2018a) by minimizing $F(p,q)$ subject to $(E_{sfs} = 0)$.

3.3.2. *Incorporating the shadow constraint into photoclinometry*

In shadowed regions, it is not appropriate to use photoclinometry because there is no shading information. However, shadows also provide information about the surface normal vectors under the shadows. The magnitude limit of the normal vectors within the shadows can be obtained by:

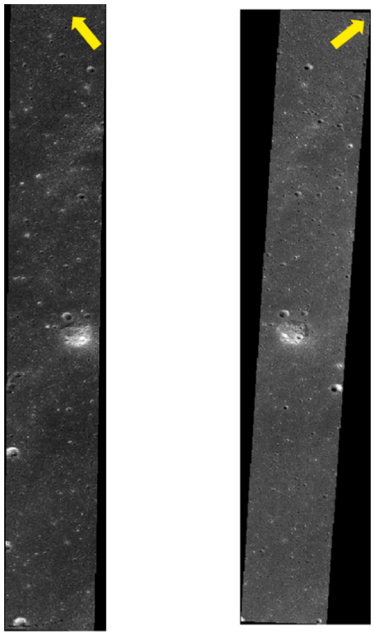

M1119207667RC M1145135367LC

Image ID	M1119207667R	M1145135367L
Slew angle (°)	14.8	0.0
Illumination azimuth (°)	154.4	233.0
Incidence angle (°)	45.7	56.0
Emission angle (°)	17.2	1.8
Resolution (m/pixel)	1.5	1.5

Fig. 11. The LROC NAC image pair within the Chang'E-5 candidate landing region. Yellow arrows indicate the illumination direction of each image. (For interpretation of the references to colour in this figure legend, the reader is referred to the web version of this article.)

$$s_{shw} = -\frac{\cos i}{\sin i} = -\frac{1}{\tan i}, \tag{15}$$

where i is the incidence angle and s_{shw} is the signed magnitude of the vector of a shadow along the illumination direction, which provides an upper limit of the normal vectors of a shadowed surface. When the normal vectors p and q are projected in the direction of the illumination, the magnitude cannot be higher than s_{shw} because, in that case, the surface would be illuminated and no longer shadowed. A straightforward way to achieve this is to force the normal vectors of each shadowed pixel to comply to s_{shw} when they are evaluated along the direction of the illumination. This constraint can be formulated as:

$$E_{shw} = \max\left(L^T \begin{bmatrix} p \\ q \end{bmatrix} - s_{shw},\ 0\right), \tag{16}$$

where $L = \begin{bmatrix} p_L \\ q_L \end{bmatrix}$ is the unit vector pointing toward the illumination source, and $L^T \begin{bmatrix} p \\ q \end{bmatrix}$ projects the normal vector (p,q) to L. For a shadowed pixel, the projected magnitude is considered to be equal to or less than s_{shw} and, hence, E_{shw} equals zero. Similar to E_{sfs}, E_{shw} is treated as an absolute constraint for the shadowed pixels. As E_{sfs} is switched off for the shadowed pixels, the optimization is to minimize $F(p,q)$ subject to $(E_{shw} = 0)$. To summarize, each pixel contains two solutions of normal vectors, one for the illuminated pixels and the other for the shadowed pixels:

$$\begin{bmatrix} p_{sfs} \\ q_{sfs} \end{bmatrix} = \arg min_{p,q} F(p, q) s.\ t.\ E_{sfs} = 0$$

$$\begin{bmatrix} p_{shw} \\ q_{shw} \end{bmatrix} = \arg min_{p,q} F(p, q) s.\ t.\ E_{shw} = 0, \tag{17}$$

where $\begin{bmatrix} p_{sfs} \\ q_{sfs} \end{bmatrix}$ is the solution derived based on the reflectance constraint $Esfs$, and $\begin{bmatrix} p_{shw} \\ q_{shw} \end{bmatrix}$ is the solution derived based on the shadow constraint E_{shw}. We assume that a shadow map of the image is available that contains the weights of the shadows for each pixel, which range from 0 to 1. The weights represent the likelihood of a pixel being shadowed based on certain shadow detection algorithm, or the fraction of a pixel that is shadowed. The final estimated normal vector is then a linear combination of $\begin{bmatrix} p_{sfs} \\ q_{sfs} \end{bmatrix}$ and $\begin{bmatrix} p_{shw} \\ q_{shw} \end{bmatrix}$ based on the weight values of the shadow map:

$$\begin{bmatrix} p_{final} \\ q_{final} \end{bmatrix} = (1 - w_{shw}) \begin{bmatrix} p_{sfs} \\ q_{sfs} \end{bmatrix} + w_{shw} \begin{bmatrix} p_{shw} \\ q_{shw} \end{bmatrix}, \tag{18}$$

where w_{shw} is the weight value of each pixel on the shadow map and $\begin{bmatrix} p_{final} \\ q_{final} \end{bmatrix}$ is the final estimated normal vector of the surface. In cases where the shadow map is a mask that has only ones for all of the shadowed pixels and zeros otherwise, $\begin{bmatrix} p_{final} \\ q_{final} \end{bmatrix}$ then solely depends on $\begin{bmatrix} p_{shw} \\ q_{shw} \end{bmatrix}$ for the shadowed regions and $\begin{bmatrix} p_{sfs} \\ q_{sfs} \end{bmatrix}$ otherwise.

3.3.3. Refining photogrammetric DEMs from photoclinometrically estimated gradients

Following the algorithm developed by Wu et al., 2018a, the elevation of each individual node on the DEM is optimized based on the photoclinometrically estimated surface gradients computed from the previous steps. The surface gradients of the DEM are obtained by finite differences:

$$p = -\frac{\partial Z}{\partial x} = \frac{1}{2h_x} \sum \begin{bmatrix} 1 & -1 \\ 1 & -1 \end{bmatrix} \circ \begin{bmatrix} Z_{x,y+1} & Z_{x+1,y+1} \\ Z_{x,y} & Z_{x+1,y} \end{bmatrix}$$

$$q = -\frac{\partial Z}{\partial y} = \frac{1}{2h_y} \sum \begin{bmatrix} -1 & -1 \\ 1 & 1 \end{bmatrix} \circ \begin{bmatrix} Z_{x,y+1} & Z_{x+1,y+1} \\ Z_{x,y} & Z_{x+1,y} \end{bmatrix}, \tag{19}$$

where h_x and h_y are the cell sizes of the DEM in the x- and y-direction, respectively, and $[\ *\ ]\circ[\ *\ ]$ is an element-wise multiplication operator. As depicted in Fig. 5, the surface normal vectors of each cell $\begin{bmatrix} p_{DEM} \\ q_{DEM} \end{bmatrix}_{i,j}$

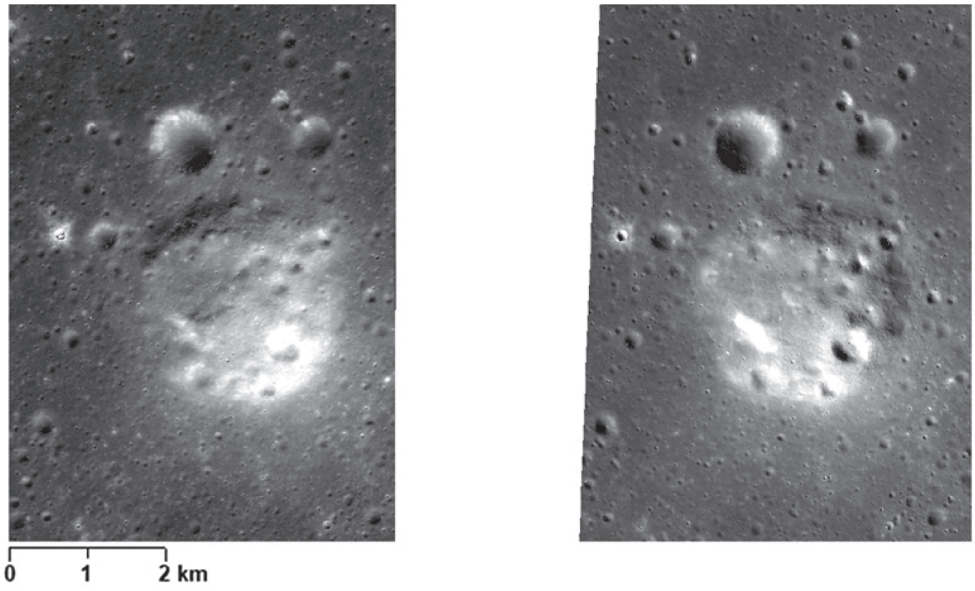

a) The base image (left) and the matching image (right)

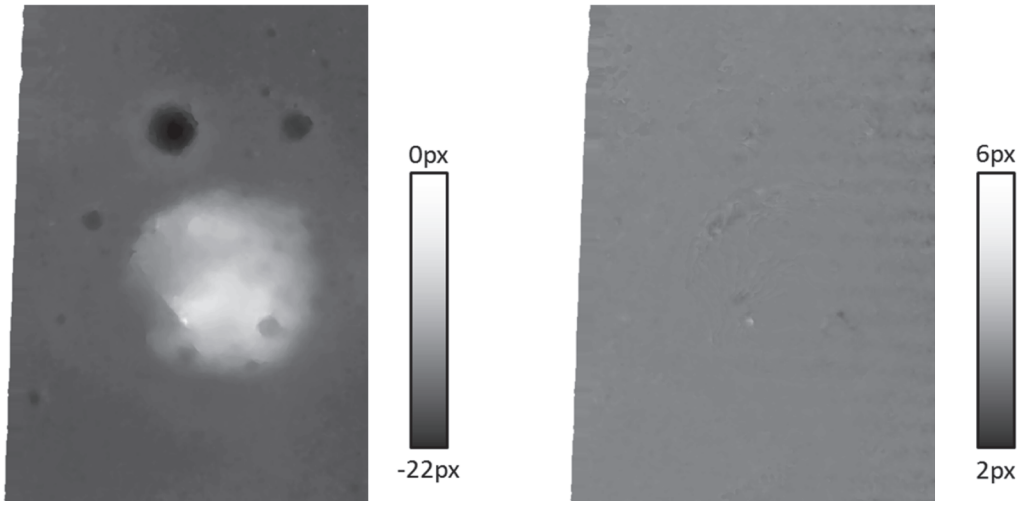

b) The x-disparity (left) and y-disparity (right) maps

Fig. 12. The epipolar images used for matching and the disparity maps generated by PAM within the Chang'E-5 candidate landing region.

are computed by the four neighboring grid nodes. Hence, the optimization of the center node $Z_{x,y}$ (the middle square in Fig. 5) is optimized in a least-squares solution according to the adjacent surface normal vectors estimated by photoclinometry. The optimization uses a relaxation strategy whereby only one DEM node is optimized and updated at a time. The refined DEM is then forwarded to the reflectance estimation, as described in Section 3.3.1, and the process iterates until the changes per iteration are negligible. Creating a DEM from the estimated normal vectors is important for the reconstruction process because it can strictly enforce integrability on the possibly non-integrable surface normal vector field and hence provide better initial estimates for the next iteration. A hierarchical approach is used to ensure that the reconstruction performance is robust. The image is first down-sampled to a predefined resolution (e.g., the resolution of the initial DEM) and the refinement process is performed accordingly. The refined DEM is then up-sampled by a factor (e.g., two) and the refinement process repeats until it reaches image resolution.

4. Experimental analysis

4.1. Experiment with LROC NAC images of the Chang'E-4 landing site

The LROC NAC images feature a high resolution, 0.5–2 m/pixel, which is favorable for the detailed 3D mapping and analysis of the landing sites for lunar missions (Speyerer et al., 2016; Wu and Liu, 2017; Hu and Wu, 2018). Fig. 6 shows a pair of LROC NAC images covering the landing site of the Chinese Chang'E-4 mission, which successfully landed on the far side of the Moon on January 3, 2019 (Wu et al., 2019). To study the topographic conditions of the landing site and the nearby environment, it is critical to have high-resolution DEMs of the region to support the topographic analysis. The stereo pair of LROC NAC images shown in Fig. 6 are those only available before and immediately after the landing. As can be seen in Fig. 6, the difference in the slew angles (convergence angles) between the images is approximately 22°, which is ideal for photogrammetric processing. However,

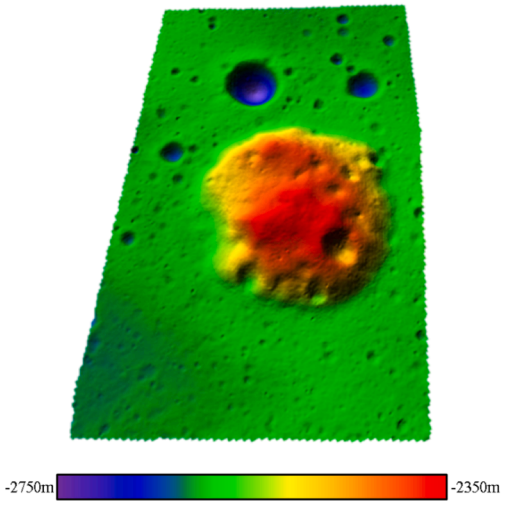

a) Reference NAC DEM (5 m/pixel)

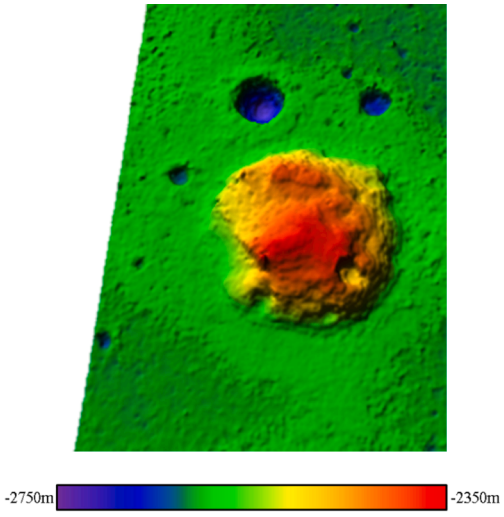

b) Photogrammetric DEM from PAM (4 m/pixel)

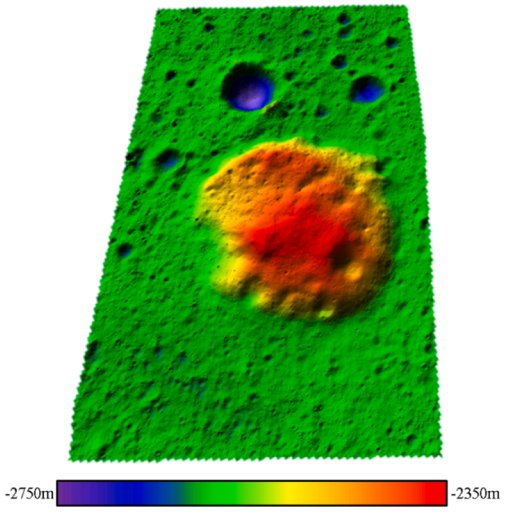

c) The integrated DEM (1.5 m/pixel)

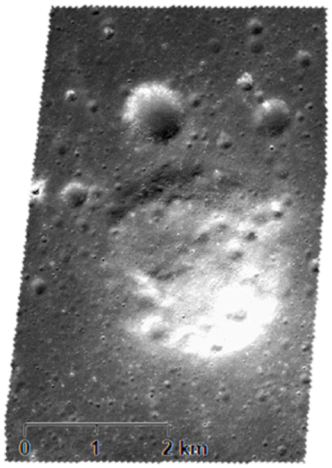

d) The ortho-image (1.5 m/pixel)

Fig. 13. 3D views of the DEMs and the corresponding ortho-image within the Chang'E-5 candidate landing region.

the illumination directions of the two images are almost opposite to each other, differing by about 164°, which implies that the conventional matching algorithms are likely to fail on this dataset. The images are associated with their EO parameters obtained from the SPICE kernels (Acton, 1996; Speyerer et al., 2016). To facilitate comparison, a reference DEM was generated independently using photogrammetry based on another stereo pair of LROC NAC images (image IDs: M1303619844LR and M1303640934LR) collected one month after the landing of Chang'E-4, which has consistent illumination conditions. The reference DEM has a resolution of 5 m/pixel, is available from the LROC Archive (http://www.lroc.asu.edu/posts/1100).

We focus our experimental analysis on the region around the Chang'E-4 landing site. Fig. 7(a) shows the image subset after epipolar rectification. The resolution of the epipolar image is resampled to 4 m/pixel, which is considered optimal for photogrammetric processing, given the resolution of the original images. The resolution of 4 m/pixel is also suitable for comparison with the reference DEM. The dimension of the image is 2000 × 1320 pixels. Due to the illumination differences, the conventional matching algorithms fail to produce any reasonable DEMs. The disparity maps are generated by matching the images using PAM and are shown in Fig. 7(b). Although the disparity maps correspond to the general topography, the detailed topographic features (e.g., small craters) are missing because they are severely shadowed in both images; these regions are outlined in blue in Fig. 7(b). In the left image, the western portions of the craters are shadowed; in the right image, the eastern portions are shadowed. Hence, when the images are analyzed during PAM matching, most of the craters are either shadowed by the left image or by the right image, and thus there is insufficient information inside the craters for matching. In general, the image pixels are required to be illuminated in both images for the best performance of PAM. In situations like this, PAM matches the portions of the craters by their illuminated surroundings such as the crater rim,

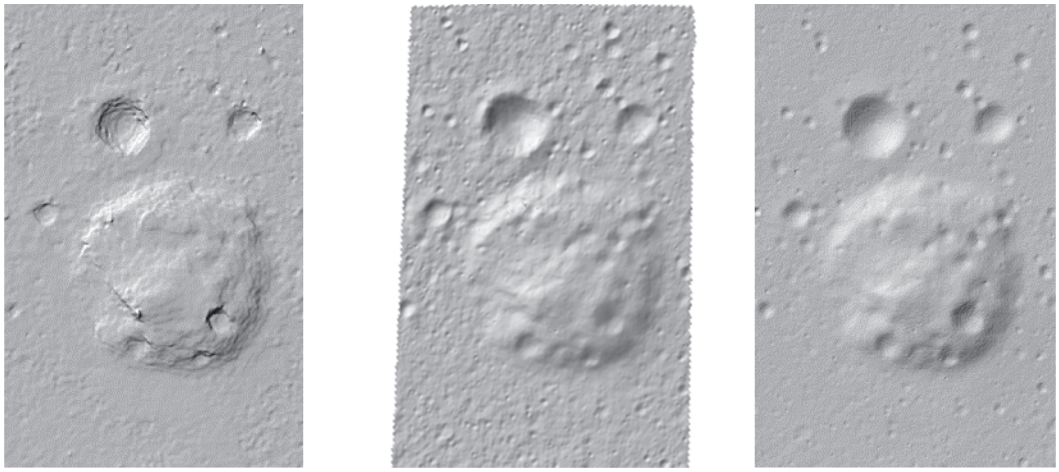

Fig. 14. The shaded relief of the DEMs within the Chang'E-5 candidate landing region.

and hence the disparities of the inner parts are replaced by those of the surroundings, leading to a smooth surface. If the craters are shaded instead of shadowed, there will be information within the craters, and their disparities can be more accurately determined by PAM. For the regions not shadowed, the disparity maps successfully retrieve their shapes.

The 3D view of the photogrammetric DEM from PAM (Fig. 8b) closely corresponds with the reference DEM (Fig. 8a) in most of the regions except for the shadowed regions. This problem can be overcome by choosing the image with the least shadows from the image pair and performing photoclinometric refinement. Fig. 8(d) shows the ortho-image generated using the photogrammetric DEM with the least shadows. The ortho-image (1.5 m/pixel) and the photogrammetric DEM (4 m/pixel) are used as inputs in the photoclinometric refinement, and an integrated DEM (1.5 m/pixel) is generated using the method described in Section 3.3, as shown in Fig. 8(c). Since the reference DEM (Fig. 8a) and the photogrammetric DEM (Fig. 8b) are produced independently using different sets of stereo images, small low-frequency deviations (about 1–3 m) in elevation, with respect to the reference DEM, can be noted on the photogrammetric DEM (Fig. 8b) and the integrated DEM (Fig. 8c). The 3D views of the DEMs (Fig. 8) and their corresponding shaded relief (Fig. 9) indicate that the integrated DEM (Fig. 8c and 9b) recovers the missing details in the photogrammetric DEM and the reference DEM.

The topography of the Chang'E-4 landing site derived from different DEMs is also compared. The integrated DEM provides the necessary information about the topography around the landing site, while no useful information can be derived from the other DEMs. Two profiles are derived from the DEMs and presented in Fig. 10. The first profile reveals two of the crater triplets surrounding the Chang'E-4 landing site. It is apparent that only the integrated DEM is able to retrieve the shape of these small craters. The relatively larger craters in Fig. 10(a) and (b) show that incorporating the shadow geometry allows precise reconstruction of the shadowed terrain where photogrammetric DEM fails to do so. There are small horizontal offsets in the shadowed regions, which likely stem from possible inaccuracies in the shadow detection.

The performance of the DEMs generated using the proposed approach is quantitatively analyzed using the root mean square error (RMSE) and the maximum absolute differences in elevations with respect to the reference DEM. The absolute deviation at the 99.5 percentile is also provided to enable a more comprehensive analysis of the performance of the approach. The indicators are summarized in Table 1. The photogrammetric DEM has an RMSE of approximately 4.3 m, an absolute maximum deviation of 38.5 m, and an absolute deviation at the 99.5 percentile of 21.7 m. The major contributor to the aforementioned error is that the image pair shadowed a significant amount of the topographic features, especially those corresponding to steeper slopes such as the crater walls. This problem is significantly improved in the integrated DEM, which has a slightly lower RMSE of 3.7 m and a significantly reduced absolute maximum difference of 19.8 m, an approximately 19 m reduction compared to the photogrammetric DEM. The 99.5 percentile also drops to approximately 11.2 m, a 10 m reduction with respect to the photogrammetric DEM. It should be noted that it is impossible to obtain a reference DEM with a better resolution of 1.5 m/pixel for comparison. However, the 5-m/pixel reference DEM can be used to provide an overall evaluation of the geometric accuracy of the DEM generated by the proposed approach.

4.2. Experiment with LROC NAC images of the candidate Chang'E-5 landing region

The Chang'E-5 mission is planned for launch around late 2019. Fig. 11 shows a stereo pair of LROC NAC images of areas within the Chang'E-5 candidate landing region (Wu et al., 2018c). There is a dome located in the middle area of the image. The difference in the slew angles between the images is about 15°, which is suitable for photogrammetric processing. However, the illumination directions of the two images differ by about 80°, indicating that conventional matching algorithms will likely fail on this stereo pair. The images are associated with their EO parameters obtained from the SPICE kernels. Similarly, a reference DEM generated from photogrammetry using other NAC images with consistent illumination conditions (image IDs: M1119207667LR and M1119228976LR) is used for comparison. The reference DEM has a resolution of 5 m/pixel.

The comparison focuses on the dome area in the middle of the image. Fig. 12 (a) shows the image subsets after epipolar-rectification. The resolution of the epipolar images is resampled to 4 m/pixel, and the dimension of the image is 1330 × 1800 pixels. After PAM, we obtain the disparity maps shown in Fig. 12(b), which largely correspond to the topography of the region. The high horizontal disparity in the middle of the image corresponds to the dome, while the dark circles above correspond to the craters. Because of the illumination configuration, most of the inner parts of the craters are illuminated in both images, and hence the effects of shadows are much less apparent than in the previous dataset. Subtle stripe patterns can be observed on the y-disparity map. A possible reason for their occurrence is that the proposed photometric stereo method (Eq. (4)) performs best when the horizontal

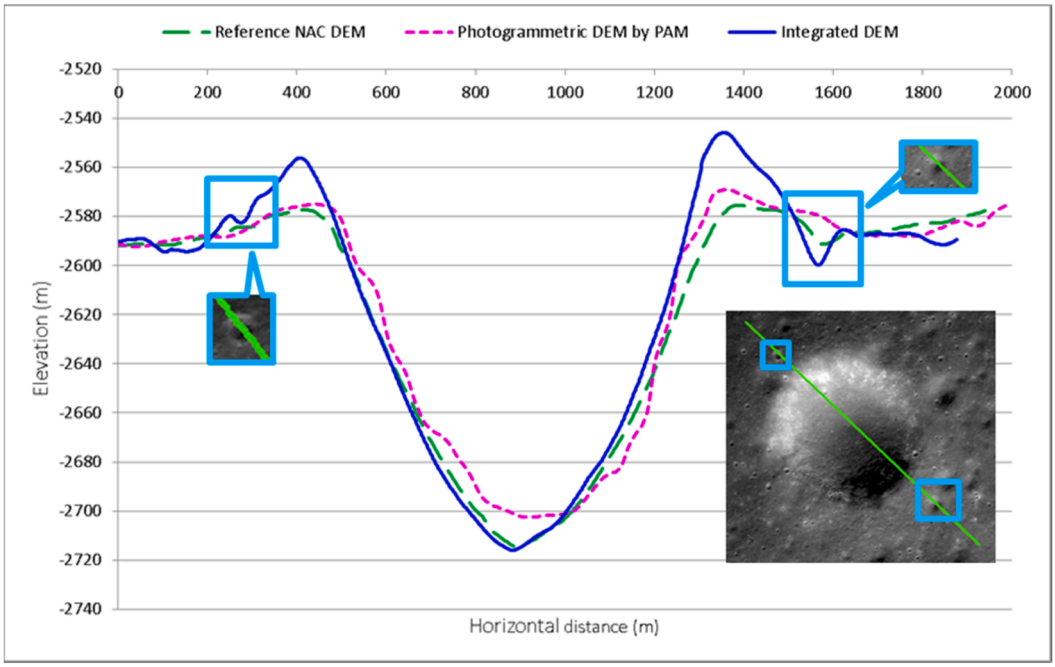

a) Profile 1

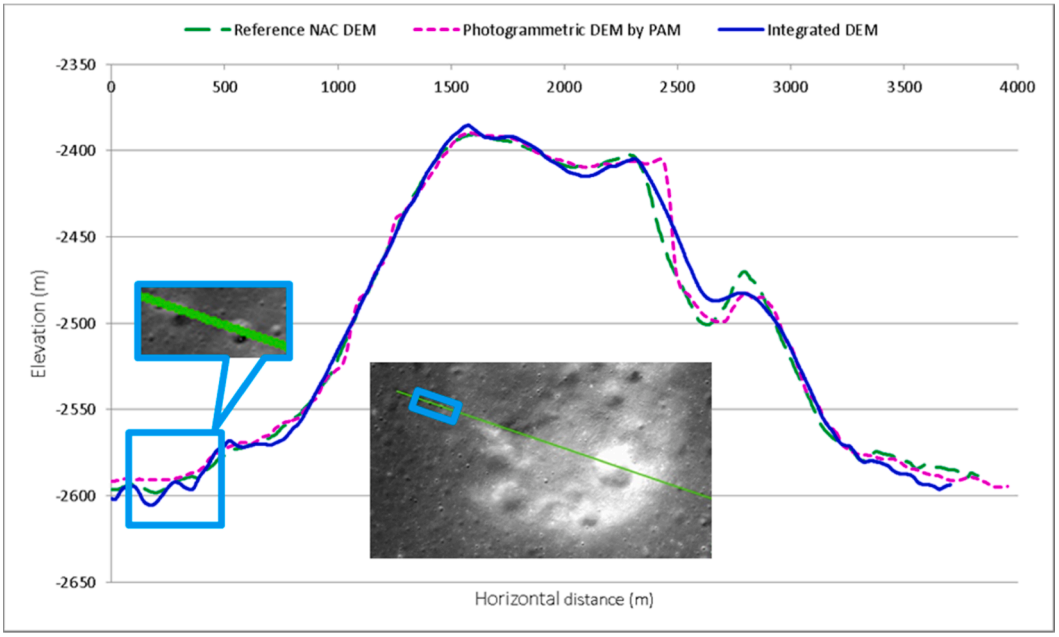

b) Profile 2

Fig. 15. Profile comparison of the DEMs within the Chang'E-5 candidate landing site. The blue boxes indicate the small topographic details revealed by the integrated DEM.

illumination differences are close to 180°, whereas in cases with illumination horizontal differences significantly less than 180° (such as about 80° in this dataset), the performance declines and becomes less sensitive to subtle changes. Nevertheless, the x-disparity is the dominating parameter for 3D reconstruction in this dataset, and most of the topographic features are revealed by the x-disparities. Hence, with this dataset, the y-disparity has a subtle effect and may contain very slight discrepancies.

Fig. 13 shows the 3D views of the reference DEM (Fig. 13a), the photogrammetric DEM (4 m/pixel) from PAM (Fig. 13b), the DEM (1.5 m/pixel) from the integrated photogrammetric and photoclinometric approach (Fig. 13c), and the ortho-image based on the photogrammetric DEM and the image EO parameters (Fig. 13d). The conventional photogrammetric routines based on SGM fail to generate any reasonable DEMs for this dataset. In contrast, although the effective resolution is not as high as the reference DEM, photogrammetric processing with PAM successfully generates a plausible DEM. Moreover, the integrated DEM successfully recovers the details better than the other DEMs, as compared with the details shown in the ortho-image, which can also be observed from the shaded relief of the DEMs as

Table 2
Comparative statistics of the DEMs within the Chang'E-5 candidate landing region.

	Photogrammetric DEM	Integrated DEM
RMSE (m)	5.76	6.55
Maximum absolute deviation (m)	54.52	45.13
Absolute deviation at 99.5 percentile (m)	18.70	24.80

shown in Fig. 14.

Two profiles are extracted from the DEMs and presented in Fig. 15. The first profile (Fig. 15a), which shows the larger crater near to the dome, demonstrates that the photogrammetric DEM is able to retrieve a precise topography while the integrated DEM is able to reconstruct the fine details. The profile of the dome (Fig. 15b) shows that the steep edges and artifacts from the photogrammetric DEM are corrected by photoclinometry. The profiles also show small craters and structures that are preserved on the integrated DEM but not on the photogrammetric DEM or the reference DEM.

The quantitative indicators of the performance of the proposed approach are summarized in Table 2. The RMSE of the photogrammetric DEM is about 5.8 m with respect to the reference DEM, while the absolute maximum is about 54.5 m and the absolute deviation at the 99.5 percentile is about 18.7 m. The pixels with large errors are usually located in the shadows and can be filtered out using operators such as a median filter. The integrated DEM has an RMSE of approximately 6.6 m, with a maximum of 45 m and an absolute deviation at the 99.5 percentile of 24.8 m. In general, the indicators are slightly higher than those of the photogrammetric DEM, except for the absolute maximum. In this case, there are slight gradual deviations in terms of very low-resolution surface gradients on the integrated DEM. This is possibly due to the spatially varying albedo, especially across the lunar dome. This can be improved by tuning the parameters or incorporating photometric stereo reconstruction for a more robust estimation of the surface.

5. Conclusions and discussion

This paper presents an integrated photogrammetric and photoclinometric approach for illumination-invariant and pixel-resolution 3D mapping of the lunar surface. The approach fuses photoclinometry and photometric stereo techniques in the photogrammetric processing in a synergistic manner. Experimental analyses of the proposed framework using actual LROC NAC images with different illumination conditions show that the proposed approach outperforms the conventional approaches. The PAM algorithm used in the proposed approach is the key to handling images with complex illumination inconsistencies, such as orthogonal illumination and opposite illumination, and images with subtle textures. Based on the resulting photogrammetric DEM, photoclinometric refinement enables pixel-wise reconstruction of the terrain surface. Photoclinometry is able to recover the topographic details missing during matching and due to shadows. The RMSE of the generated DEMs ranges from 3 to 7 m compared to the reference DEMs (i.e., DEMs generated from photogrammetry using images with consistent illumination conditions). There are occasions where the absolute error exceeds 40 m, which is mostly due to shadows or overly bright regions. These discrepancies arise because the images of these regions contain no useful information for the approach to work on, and most of the discrepancies can be corrected by photoclinometry in the subsequent refinement step. The experimental results also show that photoclinometric refinement sometimes produces small accumulative errors when the surface gradients are continuously over or underestimated. This can be improved by using tuning weights and/or introducing different constraints to the algorithm.

For the photoclinometry assisted image matching (PAM), as the relationship between the performance of photoclinometry and illumination difference of images is complex (Liu et al., 2018), specifically designed formulations and experimental analyses will be necessary in order to rigorously determine the threshold of illumination difference that is favorable for PAM. In general, PAM will be applicable for images with visually apparent illumination differences (e.g., 30° or above in incidence azimuth).

In this paper, photoclinometric refinement using a single image is used because one of the images in the dataset (e.g., the stereo pair of the Chang'E-4 landing site) is severely shadowed and is not suitable for reconstruction based on photometric stereo. However, because PAM is able to perform pixel-wise matching on images with large illumination inconsistencies, it is also possible to use photometric stereo for pixel-wise refinement as a final stage. In that case, pixel-synchronous images are needed, which can be obtained using PAM. Whether to use a single image or photometric stereo as the final refinement stage depends on the illumination conditions of the images and the user requirements.

The proposed approach has the advantage of being robust to illumination inconsistencies and subtle textures and is able to produce pixel-level resolution DEMs of the lunar surface. The approach can be used for high-resolution topographic mapping of other similar planetary bodies such as Mercury or asteroids, where substantial variations in illumination pose challenges (Preusker et al., 2017). However, for Mars, the atmospheric influence on the reflectance model needs to be investigated before it can be applied. Elements of the proposed approach may also be helpful in planetary photometric and spectral analysis. The proposed integrated photogrammetric and photoclinometric approach can also serve as a reference for high-resolution topographic mapping in Earth applications.

Declaration of Competing Interest

The authors declared that there is no conflict of interest.

Acknowledgments

The work described in this paper was funded by a grant from the Research Grants Council of Hong Kong (Project No: PolyU 152086/15E) and grants from the National Natural Science Foundation of China (Project No: 41471345 and Project No: 41671426). The work was also supported by a grant from the Hong Kong Polytechnic University (Project No: G-YBN8). The authors would also like to thank all those who worked on the archive of the LROC datasets to make them publicly available.

References

Ackermann, J., Langguth, F., Fuhrmann, S., and Goesele, M., 2012. Photometric stereo for outdoor webcams. In: IEEE Conference on Computer Vision and Pattern Recognition, Providence, Rhode Island, pp. 262–269.
Acton, C., 1996. Ancillary data services of NASA's navigation and ancillary information facility. Planet. Space Sci. 44 (1), 65–70.
Banz, C., Pirsch, P., Blune, H., 2012. Evaluation of penalty functions for semi-global matching cost aggregation. Int. Arch. Photogramm. Rem. Sens. Spatial Inf. Sci. XXXIX-B3, 1–6.
Beyer, R.A., McEwen, A.S., Kirk, R.L., 2003. Meter-scale slopes of candidate MER landing sites from point photoclinometry. J. Geophys. Res. 108 (E12) ROV 26–1.
Beyer, R.A., Kirk, R.L., 2012. Meter-scale slopes of candidate MSL landing sites from point photoclinometry. Space Sci. Rev. 170 (1–4), 775–791.
Beyer, R.A., 2017. Meter-scale slopes of candidate InSight landing sites from point photoclinometry. Space Sci. Rev. 211 (1–4), 97–107.
Foroosh, H., Zerubia, J.B., Berthod, M., 2002. Extension of phase correlation to subpixel registration. IEEE Trans. Image Process. 11 (3), 188–200.
Gaskell, R.W., Barnouin-Jha, O.S., Scheeres, D.J., Konopliv, A.S., Mukai, T., Abe, S., Saito, J., Ishiguro, M., Kubota, T., Hashimoto, T., Kawaguchi, J., Yoshikawa, M., Shirakawa, K., Kominato, T., Hirata, N., Demura, H., 2008. Characterizing and navigating small bodies with imaging data. Meteorit. Planet. Sci. 43 (6), 1049–1061.
Grumpe, A., and Wöhler, C., 2011. DEM construction and calibration of hyperspectral image data using pairs of radiance images. In: 7th International Symposium on Image and Signal Processing and Analysis (ISPA), Dubrovnik, pp. 609–614.
Grumpe, A., Belkhir, F., Wöhler, C., 2014. Construction of lunar DEMs based on

reflectance modelling. Adv. Space Res. 53, 1735–1767.
Hapke, B., 1981. Bidirectional reflectance spectroscopy: 1. Theory. J. Geophys. Res. 86 (B4), 3039–3054.
Hapke, B., 1986. Bidirectional reflectance spectroscopy: 4. The extinction coefficient and the opposition effect. Icarus 67 (2), 264–280.
Hapke, B., 2002. Bidirectional reflectance spectroscopy: 5. The coherent backscatter opposition effect and anisotropic scattering. Icarus 157 (2), 523–534.
Hapke, B., 2012. Theory of Reflectance and Emittance Spectroscopy. Cambridge University Press, Cambridge, UK.
Heipke, C., 1992. Integration of digital image matching and multiple image shape from shading. Int. Arch. Photogramm. Rem. Sens. XXIX-B3, 832–841.
Heipke, C., Oberst, J., Albertz, J., Attwenger, M., 2007. Evaluating planetary digital terrain models: the HRSC DTM test. Planet. Space Sci. 55 (14), 2173–2191.
Hirschmüller, H., 2008. Stereo processing by semi-global matching and mutual information. IEEE Trans. Pattern Anal. Mach. Intell. 30 (2), 328–341.
Horn, B.P., 1977. Understanding image intensities. Artif. Intell. 8 (2), 201–231.
Horn, B.K.P., 1990. Height and gradient from shading. Int. J. Comput. Vision 5 (1), 37–75.
Hu, H., Wu, B., 2018. Block adjustment and coupled epipolar rectification of LROC NAC images for precision lunar topographic mapping. Planet. Space Sci. 160 (1), 26–38.
Jung, J., Lee, J.-Y., Kweon, I.S., 2015. One-day outdoor photometric stereo via skylight estimation. In: IEEE Conference on Computer Vision and Pattern Recognition (CVPR), Boston, MA, pp. 4521–4529.
Kirk, R.L., 1987. III. A Fast Finite-element Algorithm for Two-dimensional Photoclinometry. Ph.D. Thesis, Caltech, pp. 165–258.
Kirk, R.L., Barrett, J.M., Soderblom, L.A., 2003a. Photoclinometry made simple? ISPRS Working Group IV/9 "Advances in Planetary Mapping" Workshop, Houston, TX.
Kirk, R.L., Howington-Kraus, E., Redding, B., Galuszka, D., Hare, T.M., Archinal, B.A., Soderblom, L.A., Barrett, J.M., 2003b. High-resolution topomapping of candidate MER landing sites with Mars orbiter camera narrow-angle images. J. Geophys. Res. 108 (E12), 8088. https://doi.org/10.1029/2003JE002131.
Konecny, G., 1985. The international society for photogrammetry and remote sensing: 75 years old, or 75 years young? Photogramm. Eng. Remote Sens. 51 (7), 919–933.
Labarre, S., Ferrari, C., Jacquemoud, S., 2017. Surface roughness retrieval by inversion of the Hapke model: A multiscale approach. Icarus 290, 63–80.
Liu, W.C., Wu, B., 2017. Photometric stereo shape-and-albedo-from-shading for pixel-level resolution lunar surface reconstruction. Int. Arch. Photogramm. Rem. Sens. Spatial Inform. Sci. XLII-3 (W1), 91–97.
Liu, W.C., Wu, B., 2018. An integrated photogrammetric and photoclinometric approach for pixel-resolution 3D modelling of lunar surface. International Archives of the Photogrammetry. Rem. Sens. Spatial Inform. Sci. XLII-3, 1117–1121.
Liu, W.C., Wu, B., Wöhler, C., 2018. Effects of illumination differences on photometric stereo shape-and-albedo-from-shading for precision lunar surface reconstruction. ISPRS J. Photogramm. Rem. Sens. 136, 58–72.
Lohse, V., Heipke, C., 2004. Multi-image shape-from-shading: derivation of planetary digital terrain models using clementine images. Int. Arch. Photogramm. Rem. Sens. XXXV (B4), 828–833.
Lohse, V., Heipke, C., Kirk, R.L., 2006. Derivation of planetary topography using multi-image shape-from-shading. Planet. Space Sci. 54 (7), 661–674.
Lowe, D., 2004. Distinctive image features from scale-invariant keypoints. Int. J. Comput. Vision 60 (2), 91–110.
McEwen, A.S., 1991. Photometric functions for photoclinometry and other applications. Icarus 92 (2), 298–311.
O'Hara, R., Barnes, D., 2012. A new shape from shading technique with application to Mars Express HRSC images. ISPRS J. Photogramm. Remote Sens. 67, 27–34.
Oren, M., Nayar, S.K., 1994. Generalization of Lambert's reflectance model. In: Proceedings of the 21st Conference on Computer Graphics and Interactive Techniques, Orlando, FL, USA, pp. 239–246.
Piechullek, C., Heipke, C., 1996. DTM refinement using multi image shape from shading. Int. Arch. Photogramm. Rem. Sens. XXXI (B3), 644–651.
Piechullek, C., Heipke, C., Ebner, H., 1998. Multi image shape from shading: Results using real aerial imagery. Int. Arch. Photogramm. Rem. Sens. XXXII (3/1), 160–167.
Preusker, F., Stark, A., Oberst, J., Matz, K.-D., Gwinner, K., Roatsch, T., Watters, T.R., 2017. Toward high-resolution global topography of Mercury from MESSENGER orbital stereo imaging: a prototype model for the H6 (Kuiper) quadrangle. Planet. Space Sci. 142, 26–37.
Salamunićcar, G., Lončarić, S., Grumpe, A., Wöhler, C., 2014. Hybrid method for crater detection based on topography reconstruction from optical images and the new LU78287GT catalogue of lunar impact craters. Adv. Space Res. 53 (12), 1783–1797.
Speyerer, E.J., Wagner, R.V., Robinson, M.S., Licht, A., Thomas, P.C., Becker, K., Anderson, J., Brylow, S.M., Humm, D.C., Tschimmel, M., 2016. Pre-flight and on-orbit geometric calibration of the Lunar Reconnaissance Orbiter Camera. Space Sci. Rev. 200 (1–4), 357–392.
Wohlfarth, K. S., Liu, W. C., Wu, B., Grumpe, A., and Wöhler, C., 2018. High resolution digital terrain models of the Martian surface: compensation of the atmosphere on CTX imagery. In: 49th Lunar and Planetary Science Conference, March 19–23, The Woodlands, Texas, Abstract No. 2498.
Wöhler, C., 2004. Shape from shading under coplanar light sources. pattern recognition. Lect. Notes Comput. Sci. 3175, 278–285.
Wöhler, C., Grumpe, A., Berezhnoy, A., Bhatt, M.U., Mall, U., 2014. Integrated topographic, photometric and spectral analysis of the lunar surface: application to impact melt flows and ponds. Icarus 235, 86–122.
Wöhler, C., Grumpe, A., Rommel, D., Bhatt, M., and Mall, U., 2017. Elemental and topographic mapping of lava flow structures in Mare Serenitatis on the Moon. In: Proc. ISPRS Int. Symp. on Planetary Remote Sensing and Mapping, Hong Kong, 2017. The International Archives of the Photogrammetry, Remote Sensing and Spatial Information Sciences, XLII-3(W1). pp. 163–170.
Woodham, R., 1980. Photometric method for determining surface orientation from multiple images. Opt. Eng. 19 (1), 139–144.
Wu, B., Liu, W.C., Grumpe, A., Wöhler, C., 2018a. Construction of pixel-level resolution DEMs from monocular images by shape and albedo from shading constrained with low-resolution DEM. ISPRS J. Photogramm. Remote Sens. 140, 3–19.
Wu, B., Zeng, H., Hu, H., 2018b. Illumination invariant feature point matching for high-resolution planetary remote sensing images. Planet. Space Sci. 152, 45–54.
Wu, B., Zhang, Y., Zhu, Q., 2011. A triangulation-based hierarchical image matching method for wide-baseline images. Photogramm. Eng. Remote Sens. 77 (7), 695–708.
Wu, B., Zhang, Y., Zhu, Q., 2012. Integrated point and edge matching on poor textural images constrained by self-adaptive triangulations. ISPRS J. Photogramm. Remote Sens. 68, 40–55.
Wu, B., 2017. Photogrammetry: 3D from imagery. In: Richardson, D., Castree, N., Goodchild, M.F., Kobayashi, A., Liu, W., Marston, R.A. (Eds.), The International Encyclopedia of Geography. John Wiley & Sons Ltd, New York, NY, pp. 1–13.
Wu, B., Liu, W.C., 2017. Calibration of boresight offset of LROC NAC imagery for precision lunar topographic mapping. ISPRS J. Photogramm. Remote Sens. 128, 372–387.
Wu, B., Huang, J., Li, Y., Wang, Y., Peng, J., 2018c. Rock abundance and crater density in the candidate Chang'E-5 landing region on the Moon. J. Geophys. Res. Planets 123 (12), 3256–3272.
Wu, B., Li, F., Hu, H., Zhao, Y., Wang, Y., Xiao, P., Li, Y., Liu, W., Chen, L., Ge, X., Yang, M., Xu, Y., Ye, Q., Wu, X., Zhang, H., 2019. Topographic and geomorphological analysis of the Chang'E-4 landing site on the far side of the Moon. Earth Space Sci.